Title

Automatic Attribute Profiles

Journal

IEEE Transactions on Image Processing, 26(4)

ISSN

1057-7149

Authors

Cavallaro, Gabriele

Falco, Nicola

Mura, Mauro Dalla

et al.

Publication Date

2017-04-01

DOI

10.1109/tip.2017.2664667

Peer reviewed

Automatic Attribute Profiles

Gabriele Cavallaro, *Member, IEEE,* Nicola Falco, *Member, IEEE,*
Mauro Dalla Mura, *Member, IEEE,* and Jón Atli Benediktsson, *Fellow, IEEE*

***Abstract*—Morphological attribute profiles are multilevel decompositions of images obtained with a sequence of transformations performed by connected operators. They have been extensively employed in performing multi-scale and region-based analysis in a large number of applications. One main, still unresolved, issue is the selection of filter parameters able to provide representative and non-redundant threshold decomposition of the image. This paper presents a framework for the automatic selection of filter thresholds based on Granulometric Characteristic Functions (GCFs). GCFs describe the way that non-linear morphological filters simplify a scene according to a given measure. Since attribute filters rely on a hierarchical representation of an image (e.g., the Tree of Shapes) for their implementation, GCFs can be efficiently computed by taking advantage of the tree representation. Eventually, the study of the GCFs allows the identification of a meaningful set of thresholds. Therefore, a trial and error approach is not necessary for the threshold selection, automating the process and in turn decreasing the computational time. It is shown that the redundant information is reduced within the resulting profiles (a problem of high occurrence, as regards manual selection). The proposed approach is tested on two real remote sensing data sets, and the classification results are compared with strategies present in the literature.**

***Index Terms*—automatic attribute profiles, filter parameter selection, tree representation, mathematical morphology, remote sensing, image processing.**

I. Introduction

TAKING into account the spatial information of images (e.g., the contextual relations among neighboring pixels, shape characteristics of regions, scale, etc) has proved to be beneficial for the interpretation of the image content in many application domains, such as astronomy [1], medical imaging [2] and remote sensing [3], [4]. However, modeling and retrieving spatial features is a challenging task. In this context, mathematical morphology (MM) [5] has been playing an important role, since it provides a wide set of operators that perform contextual image transformations. These transformations are able to probe the image content and can be useful to infer hints on spatial characteristics of objects in the image (e.g., geometry, shape, and edges) according to the output of the transformations. In remote sensing, the MM finds its main applications in image filtering, segmentation and measurements [6]. In order to solve such problems, pixel-based approaches are not usually considered as good candidates. To meet this need, the MM framework contains useful tools that provide tree-based image representations, i.e., a representation of the image content in a tree structure in which each node corresponds to a region in the image. Tree representations are an important solution for many image processing applications, e.g., pattern recognition in astronomical imaging [7], representation of different types of multivariate images (e.g., color natural images, multimodal medical imaging, etc.) [8], detection and localization of objects in images [9], etc. Tree representations of images can be divided into two groups [10]: hierarchies of segmentation (i.e., hierarchy of image partitions such as minimum spanning tree (MST) [11], alpha-tree [12], binary partition tree (BPT) [13]) and threshold decompositions (i.e., hierarchy of regions such as min- and max-tree [14], [15], Tree of Shapes (ToS) [16]). The difference between a hierarchy of segmentation and tree based on the threshold decomposition is that when taking a horizontal cut, the former leads to a partition of the image (i.e., set of non-overlapping regions whose union covers the entire image domain) whereas the latter to a set of regions representing a partial partition. In general, these representations enable multi-scale analysis of objects and spatial analysis of the image organization [17].

The work presented in this paper deals with the threshold decomposition representations, which are composed of a set of regions organized in a hierarchical way. Threshold decompositions have been popularized by connected operators, such as attribute filters [5] [18], which have been extensively used for the modelling of spatial information of images from remote sensing [19], astronomy [20] and medical scanning [21] [22]. Attribute filters are edge-preserving and flexible operators since they preserve the contours of the processed objects and rely on many different spatial measures (i.e., attributes). For example, one can express the objects to be filtered out through a criterion (attribute) that tells the connected components (i.e., flat zones [23]) whether to be preserved or removed. This attribute can be increasing (e.g., the *area* of the component) or non-increasing (e.g., *standard deviation*, *moment of inertia*, etc.). A given attribute causes a specific filtering transformation, extracting contextual information that is complementary to the one extracted by other attributes. The possibility to perform a multi-attribute analysis (i.e., attribute filters built by employing different attributes) enriches the extraction of spatial arrangement and improves the discrimination between different structures. However, the analysis of a scene becomes more challenging when heterogeneous structures populate

G. Cavallaro is with the Juelich Supercomputing Centre, Wilhelm-Johnen-Straße, 52428 Juelich, Germany (e-mail: g.cavallaro@fz-juelich.de).

N. Falco is with the Climate & Ecosystems Division, Lawrence National Berkeley Laboratory, Berkeley, CA 94720, USA (e-mail: nicolafalco@lbl.gov).

M. Dalla Mura is with the Univ. Grenoble Alpes, CNRS, GIPSA-lab, F-38000 Grenoble, France (e-mail: mauro.dalla-mura@gipsa-lab.grenoble-inp.fr).

J. A. Benediktsson is with the Faculty of Electrical and Computer Engineering, University of Iceland, Reykjavik, Iceland (e-mail: benedikt@hi.is).

This research was supported in part by the EU FP7 Theme Space project North State, by the program J. Verne 2014 under Project 31936TD, and by the INS2I JCJC 2015 under project "IDES". The authors are grateful to F. Pacifici for providing the Rome data set, and to Prof. P. Gamba for the Pavia data set.

the scene. In this case, a multi-level decomposition of the original gray-level image obtained by applying a sequence of attribute filters according to a pre-defined set of filter thresholds is preferable. The result of this operation are the so-called attribute profiles (APs) [24] or self-dual attribute profiles (SDAP) [25], [26], in case of min- and max-tree or ToS, respectively. Due to the aforementioned properties, these operators and their multi-channel and multi-attribute extensions [27] [28] have gained an increasing popularity. They have been exploited mainly in remote sensing (e.g., classification [29]–[32], data fusion [33] and change detection [34], [35]) and medical imaging processing (e.g., segmentation of computed tomographic images [36]).

Multi-attribute profiles can extract complementary information and effectively model the spatial context. However, the filter parameter selection (i.e., a set of values used in the filtering in order to construct a profile) remains one of the main operational issues, affecting their usability in different applicative contexts, such as feature extraction, visual exploration, compression, etc. Although the parameter tuning is unavoidable, most of the works dealing with morphological operators for multi-level analysis do not tackle this issue, whereas the use of similar parameters, even for different case studies, seems to be the general strategy. In the literature, only few works addressing this issue can be found [37]–[40]. Since the morphological analysis is data dependent, the identification of the suitable threshold sets should be based on empirical searching. However, such strategy can be time-consuming and perceptively not trivial.

Focusing on this issue, this paper presents a novel automatic approach for the selection of filter parameters[1] for morphological attribute profiles. The proposed method aims to provide a data-adaptive and user-independent strategy to identify a suitable threshold set for computing profiles that need to be both representative (i.e., containing salient structures of the image) and non-redundant (i.e., objects are present only in one or few levels of the profile). The method exploits the threshold decomposition representation of an image, from which can be derived useful information related to the actual range of the attribute values. This design choice is extremely important since no filtering has to be performed to the image in order to carry out the thresholds selection. The main idea underlying the automatic selection procedure is to identify a set of threshold values that approximate a given behavior of the multi-level decomposition. For this purpose, the concept of *granulometric characteristic functions* (GCFs) is here introduced as an extension of the conventional notion of granulometry [41]. We recall that a granulometric curve (or granulometry) is a representation of the distribution of sizes in an image based on the intermediate residuals of a sequence of increasingly coarser anti-extensive or extensive morphological filters (a granulometric family) [42, Ch. 1.4.2]. A GCF is defined as a mapping from a grayscale image to a scalar value which computes a global measures of the image. When considering a set of images resulting from the application of a sequence of increasingly coarser filters, the GCF shows the variation of the underlying measure with respect to the increasing filtering effect. Granulometries are useful descriptors for texture analysis and for gathering information on the characteristics of objects in the image [41]. The conventional granulometry uses the volume of the image (i.e., the sum of the grayvalues of all pixels in the scene) as measure. However, several measures other than the sum of graylevels can be considered for defining functions able to represent the effects of a sequence of filters from different aspects. For example, in this work we propose two additional GCFs that are not based on graylevels (i.e., the number of pixels and regions that are affected by a filtering). However, other definitions are possible according to which characteristic one wants to monitor in a filter-based decomposition of the image. Since the morphological filters considered in this work are efficiently implemented on a hierarchical representation of the image, the computation of GCFs that we propose also exploits the tree representation. This is an extremely interesting feature of the proposed selection strategy since the GCFs can be efficiently computed directly on the tree, without requiring any prior filter step.

For the automatic threshold selection we proceed as follows. Similarly to [40], in this work, the set of thresholds that best approximates the GCF computed on the full set of thresholds is sought. The main assumption is that the distribution of a given *measure* along the profile can be extracted and approximated by using a subset of selected thresholds. An adaptive regression model [43] approximates the original GCF for an increasing number of thresholds. Eventually, the final set of thresholds is identified when the estimation error between the original and the approximated GCFs is minimized.

To summarize, the contributions of this paper are threefold: i) a framework for the automatic and efficient selection of morphological attribute filters' parameters, which does not require any actual filtering of the image; ii) the definition of Granulometric Characteristic Functions as a generalization of the conventional granulometric curve based on grayvalues; and iii) a strategy based on regression for the selection of thresholds from GCFs.

The remainder of the paper is as follows: In Section II an overview on the strategies proposed in the literature is presented. Section III provides a briefly introduction to the morphological operators and tree representations. In Section IV the proposed method is described, while the experiment analysis is shown in Section V. Section VI concludes the paper, discussing the findings of the study.

II. Related Work

There have been only few attempts to solve the problem of the filter threshold selection in mathematical morphology. In general, a common approach is to derive a reasonable set of thresholds based on the field-knowledge of the scene. This requires a visual inspection of the scene under investigation, followed by a manual selection. This approach often requires multiple filtering tests to select the appropriate final threshold set. Depending on the considered attribute and the complexity

[1]The parameters of the morphological filters are hereafter referred to also as filter thresholds, since attribute filters are based on the evaluation of a binary criterion which compare an attribute value against a given threshold

of the scene, this process can be computationally expensive and time consuming.

To the authors' best knowledge, the first automatic approach aimed at decreasing the manual intervention was proposed in [37], where a vector of thresholds was derived by computing a given attribute on each object extracted by a preliminary clustering or classification computed on the original scene. The final set of thresholds was identified by clustering the threshold vector and selecting for each cluster the threshold corresponding to the minimal attribute value. The method provided better or similar results to the manual selection. A drawback of the approach is represented by the possible inconsistency between the attribute values of the connected components extracted by the classification map and those represented by the tree, making the approach very sensitive to variations in the pre-classification map.

In a supervised classification scenario, an automatic procedure for the threshold selection of the *standard deviation* attribute was proposed in [38]. The selected thresholds were identified based on a statistical analysis of the available training samples. Similar approach was extended to the *area* attribute in [39]. These procedures identify a large set of thresholds, providing high dimensional profiles that intrinsically contain redundant features, and thus, requiring a further dimensionality reduction procedure in order to avoid the raising of the Hughes' phenomenon.

An interesting strategy was proposed in [40], where the filter thresholds of the *area* profile were selected based on the analysis of the characteristic function of the pattern spectrum [44], [45], which corresponds to the probability density function of the granulometric curve of the *area* profile, i.e., a curve related to the size distribution of the structures in the image [41]. In particular, the selected thresholds were those whose characteristic function best approximated the one obtained by considering a larger set of thresholds. The method required an initial set of thresholds, which was manually defined prior to the filtering. The selection was then based on the sampling of the original characteristic function with a constant rate. In this case, a number of filtered images (potentially with all possible thresholds) were produced in order to compute both the original and the approximated granulometric curves, resulting in a computationally non-efficient strategy.

What associates all the aforementioned methods is that they might not exploit the full information contained in the tree representations. For instance, instead of exploiting the nodes information they involve additional statistical learning methods (e.g., supervised/unsupervised classification, feature extraction). The idea of this work started by a simple consideration: the filtered images that compose a profile are computed by pruning a tree. A simple and effective threshold selection method can be based entirely on morphological information contained in the tree.

III. Theoretical Background

A. Trees based on threshold decomposition

This section reviews three tree representations based on threshold decomposition of the image, namely, the min- and max-tree (i.e., component trees) and the Tree of Shapes (ToS). Component trees were introduced by Jones [14], [46] as efficient image representations that enable the computation of advanced morphological filters in a simple way. These trees are actually hierarchical structures that encode the threshold sets and their inclusion relationship and allow efficient implementations of connected filters.

More formally, let $f : \Omega \rightarrow E$ be a discrete two-dimensional grayscale image, defined on a spatial domain $\Omega \subseteq \mathbb{Z}^2$ and taking values on a set of scalar values $E \subseteq \mathbb{Z}$. For any $\lambda \in \mathbb{Z}$, a lower $\mathcal{L}(f)$ and upper $\mathcal{U}(f)$ threshold set is defined by:

$$\mathcal{L}(f) = \{x \in \Omega, f(x) < \lambda\}, \tag{1}$$

$$\mathcal{U}(f) = \{x \in \Omega, f(x) > \lambda\}, \tag{2}$$

Let $\mathbb{P}(\Omega)$ be the power set of all the possible subsets of Ω. Given $X \in \Omega$, the set of connected components of X is denoted as $\mathcal{C}(X) \in \mathbb{P}(\Omega)$. If $\leq$ is a total relation, any two connected components $X, Y \in \mathcal{C}(\mathcal{L}(f))$ are either disjointed or nested. The min-tree and max-tree structures represent the components in $\mathcal{L}(f)$ and $\mathcal{U}(f)$ respectively with their inclusion relations. For example, Fig. 2(c) shows the max-tree structure of the image in Fig. 2(a). The arrows in denote the parent relation between the nested connected components that are identified in Fig. 2(b).

The Tree of Shapes (also known as topographic map), is a hierarchical representation of a gray-level image in terms of the inclusion of its level lines. The ToS is a morphological self-dual representation of the connected components within an image (i.e., zones enclosed by an isolevel line). Since it is self-dual, it makes no assumption about the contrast of objects (either light object over dark background or the contrary). The ToS can be interpreted as the result of merging the min- and max-tree [15] into a single tree. It was firstly introduced by Monasse *et al.* [47], where the structure was computed with the Fast Level Line Transform (FLLT) algorithm: it first computes the pair of dual component trees and then obtains the ToS by merging both trees. Afterwards, Caselles *et al.* [48] introduced the Fast Level Set Transform algorithm (FLST), which relies on a region-growing approach to decompose the image into shapes. An operation called saturation is applied to the connected components, resulting in flat regions obtained by progressively merging nested regions. Specifically, the algorithm extracts each branch of the tree starting from the leaves and growing them up to the root until only a single flat region is reached. Song *et al.* [49], proposed to retrieve the ToS by building the tree of level lines and exploiting the interior of each level line. Recently, Geraud *et al.* [50] proposed a new algorithm to compute the ToS in order to reduce the computational complexity and overcome the restriction to only 2D images of the previous methods. The algorithm computes the ToS with quasi-linear time complexity when data quantification is low (typically 12 bits or less) and it works for nD images. Moreover, Crozet *et al.* [51] presented the first parallel algorithm to compute the morphological ToS based on the previous algorithm [50].

Described more formally, given the set $X \in \Omega$ let ∂X be the border of X and $\bar{X}$ the complementary of X. The hole-filling operator $\mathcal{H} : \mathbb{P}(\Omega) \rightarrow \mathbb{P}(\Omega)$ is defined by:

$$\mathcal{H}(X) = \Omega \setminus \mathcal{C}(\bar{X}, \partial X) \tag{3}$$

where $\mathcal{C}(\bar{X}, \partial X)$ is the *connected component* of $\bar{X}$ linking with the image border. Given the operator $\mathcal{H}$, a shape is any element of the set:

$$\mathcal{S} = \{\mathcal{H}(\mathcal{L})\}_\lambda \cup \{\mathcal{H}(\mathcal{U})\}_\lambda \tag{4}$$

If $\leq$ is total, any two shapes are either disjointed or nested, hence the cover of $\mathcal{S}, \subseteq$ makes the ToS. The definition of the shapes as hole-filled *connected components* of the lower $\mathcal{L}(f)$ and upper $\mathcal{U}(f)$ threshold set proofs that the ToS can be seen as a merge of the min- and max-tree. However, the hole-filling operation creates shapes within neither to the min-tree nor to the max-tree.

B. Attribute filters

The way $\mathcal{C}$ is defined leads to different tree representations (see previous section) and hence distinct partition π_f (i.e., set of connected components of f) of the spatial domain Ω. If we consider a connected operator ψ, by definition it will operate on f only by merging the connected components of the given set $\mathcal{C}$ [23]. Thus, the result of the filtering will be a new partition π_ψ that is coarser (i.e., containing fewer regions) than the initial one: $\pi_f \sqsubseteq \pi_{\psi(f)}$ meaning that for each pixel $p \in \Omega$, $\pi_f(p) \subseteq \pi_{\psi(f)}(p)$ [42, Ch. 7]. The coarseness of the partition generated by a connected operator is determined by a threshold λ (i.e., a size-related filter threshold). Given two instances of the same connected operator with different filtering thresholds, ψ_{λ_i} and ψ_{λ_j}, which we denote for simplicity as ψ_i and ψ_j, respectively, there is an ordering relation between the resulting partitions: $\pi_{\psi_i} \sqsubseteq \pi_{\psi_j}$ given $\lambda_i \leq \lambda_j$. Among the different types of connected operators, attribute filters have largely diffused. Attribute filters remove connected components in $\mathcal{C}$ according to an attribute $\mathcal{A}$ that is computed on each component. In greater detail, the value of an attribute $\mathcal{A}$ is evaluated on each connected component in $\mathcal{C}$ and this measure is compared with a reference threshold λ in a binary predicate T_λ (e.g., $T_\lambda := \mathcal{A} \geq \lambda$). An attribute can be increasing (e.g., the area of the component) or non-increasing (e.g., standard deviation, moment of inertia, etc.). In the former, the increasingness of $\mathcal{A}$ leads to an attribute closing or opening (min-tree and max-tree, respectively). The tree filtering is rather straightforward, since it is performed by pruning the nodes whose attribute function $\mathcal{A}$ is under a given threshold, which can be seen as an attribute thresholding. In the latter, the non-increasingness of $\mathcal{A}$ leads to attribute thinnings and thickenings. Specific filtering and restitution rules have been defined in [15] [45] for non-increasing attributes that can be categorized in two groups: pruning and non-pruning strategies. In general terms, if the predicate is true the component is maintained, otherwise it is removed. According to the attribute considered, different filtering effects driven by characteristics such as the regions' scale, shape or contrast can be obtained, leading to a simplification of the image.

C. Attribute profiles

Let us consider a family of L connected operators ψ computed considering a sequence of L either increasing or decreasing values of the filter threshold $\Lambda = \{\lambda_i\}_1^L$ that we call it a *profile* $\mathcal{P}_\psi := \{\psi_i\}_1^L$. Considering the entries of a profile, the absorption property holds on the resulting partitions such that $\psi_j\psi_i$ will lead to π_{ψ_j} for $i \leq j$. So filtered results can be ordered sequentially.

In this work, we will focus on profiles built with attribute filters, so called *attribute profiles* (APs). Profiles considering attribute filters were initially proposed for the analysis of remote sensing images in [24]. By considering a max and a min-tree, attribute opening and closing profiles were defined, respectively as:

$$\mathcal{P}_\gamma = \{\gamma^{T_0}, \gamma^{T_{\lambda_1}}, \ldots, \gamma^{T_{\lambda_L}}\}, \tag{5}$$

$$\mathcal{P}_\phi = \{\phi^{T_0}, \phi^{T_{\lambda_1}}, \ldots, \phi^{T_{\lambda_L}}\}, \tag{6}$$

where γ^T and ϕ^T represent the attribute opening and closing, respectively, $\{T_i\}$ is a criterion evaluated on the set of thresholds Λ and $\phi^{T_0}(f) = \gamma^{T_0}(f) = f$, which is the original image. By denoting with $\mathcal{P}_\phi^-$ the closing profile taken in reverse order (such that each entry is greater or equal than the subsequent one), in [24] its concatenation with an attribute opening profile was named Attribute Profile (AP):

$$\text{AP} = \{\mathcal{P}_\phi^- \setminus \phi^{T_0}, \mathcal{P}_\gamma\}. \tag{7}$$

The AP is composed of $2L+1$ images (L closings, the original image and L openings).

Analogously, when considering the contrast invariant operator ρ based on the inclusion tree, the profile $\mathcal{P}_\rho$, named *Self-Dual Attribute Profile* (SDAP) [25], [26], can be obtained:

$$\mathcal{P}_\rho = \{\rho^{T_0}, \rho^{T_{\lambda_1}}, ..., \rho^{T_{\lambda_L}}\}, \tag{8}$$

with $\rho^{T_0}(f) = f$.

IV. Proposed Approach for Automatic Threshold Selection

A. Definition of Granulometric Characteristic Function

The proposed automatic threshold system is based on the definition of a descriptive function that globally quantifies the filtering effect on gray-level image due to the image transformation performed by a connected operator ψ. Being inspired by the concept of granulometric curves, which show the interaction of the size of the image structures with the filters when the filter threshold varies, we extend the granulometry definition by considering other characteristics that can be measured to provide information on the effect of increasingly coarser filtering. Exploiting the tree representation, a *measure* $\mathcal{M}(\psi)$, representing a specific aspect of the filtering effect we want to measure, can be easily computed at each threshold value, resulting in the definition of a *granulometric characteristic function* (GCF), which is formally defined as:

$$\text{GCF}(\mathcal{P}_\psi(f)) = \{\mathcal{M}(\psi_i)\}_{i=1}^L. \tag{9}$$

Thus, if $\mathcal{M} : f \rightarrow \mathbb{R}$, $\text{GCF}(\mathcal{P}_\psi(f))$ leads to L scalar values (one for each value of threshold extracted from the tree representation).

In this study, we present three definitions of GCFs based on the following three *measures* $\mathcal{M}$:

1) Sum of gray-level values: Similarly to the conventional granulometry, this measure provides information related to the effect of the filtering with respect to the changes in terms of gray-levels that are produced in the image.

$$\text{GCF}_{val}(\mathcal{P}_\psi(f)) = \left\{\sum |f - \psi_i(f)|\right\}_{i=1}^{L}. \quad (10)$$

When attribute filters are applied on the ToS, the sum of gray-level values might not be meaningful since the hierarchy in which the nodes are organized is not driven by an ordering relation among gray levels (i.e., as for min-tree and max-tree). The nodes of the ToS follow the inclusion relationship of the regions and hence the interpretation of the GCF is not straightforward. For instance, in Fig. 1 the effect of the filtering applied on the image is not accounted by the GCF measure since there is no change in the total sum of gray values before and after the filtering.

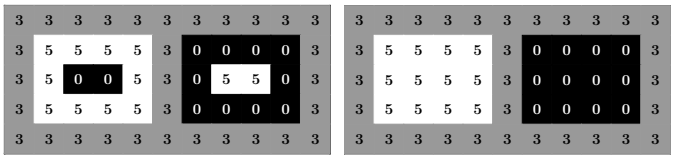

(a) (b)

Fig. 1. Attribute filter computed on the ToS: $T = \mathcal{A}(area) \leq 2$. Original image (a) and filtered image (b). In both images, the sum of the gray-level values is equal to 153.

2) Number of changed pixels: This measure provides information on the number of pixels that change gray-value at different filtering. The obtained GCF results more sensitive to changes in the spatial extent of the regions rather than in gray-levels.

$$\text{GCF}_{pix}(\mathcal{P}_\psi(f)) = \{\text{card}[f(p) \neq \psi_i(f)(p)], \forall p \in E\}_{i=1}^{L}, \quad (11)$$

where card$[\cdot]$ denotes the cardinality of a set.

3) Number of changed regions: This measure extracts information on the number of connected components that are affected at each filtering level. It is topological invariant to both the spatial extent and gray-level variations induced by the filtering.

$$\text{GCF}_{reg}(\mathcal{P}_\psi(f)) = \{\text{card}[\mathcal{C}(f)] - \text{card}[\mathcal{C}(\psi_i(f))]\}_{i=1}^{L}. \quad (12)$$

The considered measures increase for progressively coarser filters, providing monotonic increasing GCFs. An example of the extraction of a GCF is shown in Fig. 3, where a toy image is used. Starting from the tree representation of the image, which, in this case, is a max-tree, the GCF is obtained by considering the number of regions as measure.

It is worth noting that other measures able to describe specific characteristics of the filtering effects could be also considered and implemented for the definition of more GCFs.

B. Automatic threshold selection

1) Purpose: The problem we want to address can be formulated as the identification of a subset $\hat{\Lambda} = \{\hat{\lambda}_i\}_{z=1}^{\hat{L}}$ among the set of all possible values of λs, $\bar{\Lambda} = \{\lambda_i\}_{i=1}^{L}$, with $\hat{L} \ll L$. The full set $\bar{\Lambda}$ is extremely scene dependent and can potentially be very large making the problem of selecting the subset $\hat{\Lambda}$ more complicated, since the full set is not readily accessible. A possible strategy for the selection relies on the computation of a profile by considering a relatively large number of λs (considering all of them in real scenarios is impractical) and prune the profile by selecting some of filtered images and related filter thresholds so defining $\hat{\Lambda}$. However, such an approach is limited by the need of generating the filtered images in order to perform the selection and by the lack of guarantee that all possible thresholds are considered for selection. Here we propose to consider the GCFs defined in Sec. IV-A in order to select those values λs that lead to "significant" changes in the effect of the filters (as measured by the considered GCF). A similar approach was first exploited in [40], where granulometric curves were used for estimating a pre-defined sub-set of values of λ that generate salient filtered images (see Section II). The main advantage of the proposed method is the use of tree representation of the image (augmented with the values of the attributes for each node), which allows us to obtain prior information on the image decomposition, such as the full set $\bar{\Lambda}$ (i.e., all possible values of λ), to compute a GCFs prior any filtering. In particular, each node, which maps a region of spatially connected pixels in the image, gives information related to the value of attributes, gray-level and number of pixels. Such information is exploited for the computation of the GCFs.

2) Proposed solution: Similarly to [40], in the proposed approach, the set $\hat{\Lambda}$ of the selected thresholds corresponds to the one that best approximates a GCF computed on the set $\bar{\Lambda}$. By approximating a GCF curve, we assume that the distribution of the measure $\mathcal{M}$ that underlies the GCF can be extracted and approximated by using the selected $\hat{L}$ thresholds. The approximated GCF curve, hereafter GĈF, is obtained by using a piecewise linear regression approach [43][2] which C++ implementation is freely available.

The method implements an adaptive segmentation approach for time-series where segmentation points (or breakpoints) divide the time series into intervals (or segments). In our case, time-series represent sequences of data points $(x_0, y_0), \ldots, (x_{n-1}, y_{n-1})$, with x_i representing the threshold i and (y_i) the correspondent GCF's intensity. A polynomial function is exploited to approximate each interval according to a chosen model that describes the interval itself (e.g., constant, linear, etc.). The segmentation error is estimated by computing the Euclidean (l_2) norm between the interval and its polynomial approximation. In our approach, the segmentation of the original GCF is achieved by considering constant and linear models. This would drive the segmentation to have segments that cover intervals characterized by a linear behaviour and have segmentation points where a change in

[2]The C++ implementation used in this work is freely available at http://lemire.me/fr/abstracts/SDM2007.html

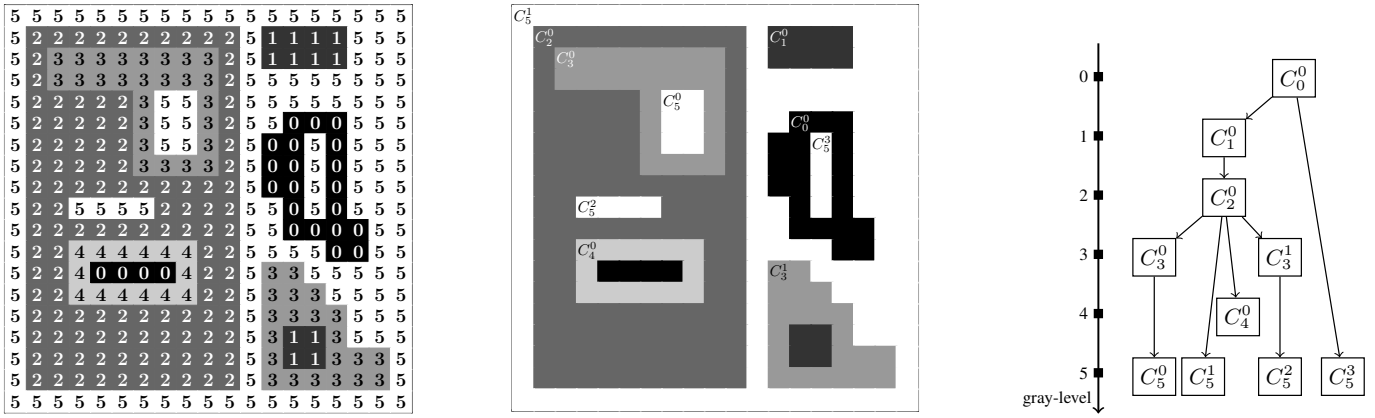

(a) (b) (c)

Fig. 2. Example of max-tree representation derived by a toy image. (a) Toy image where for each pixel the grey-value is shown. (b) The iso-level regions, which represent the connected regions, are identified. (c) The structure of the max-tree that describes the image in its components C (note that the subscript represents the gray-level while the superscript uniquely identifies the component within the gray-level).

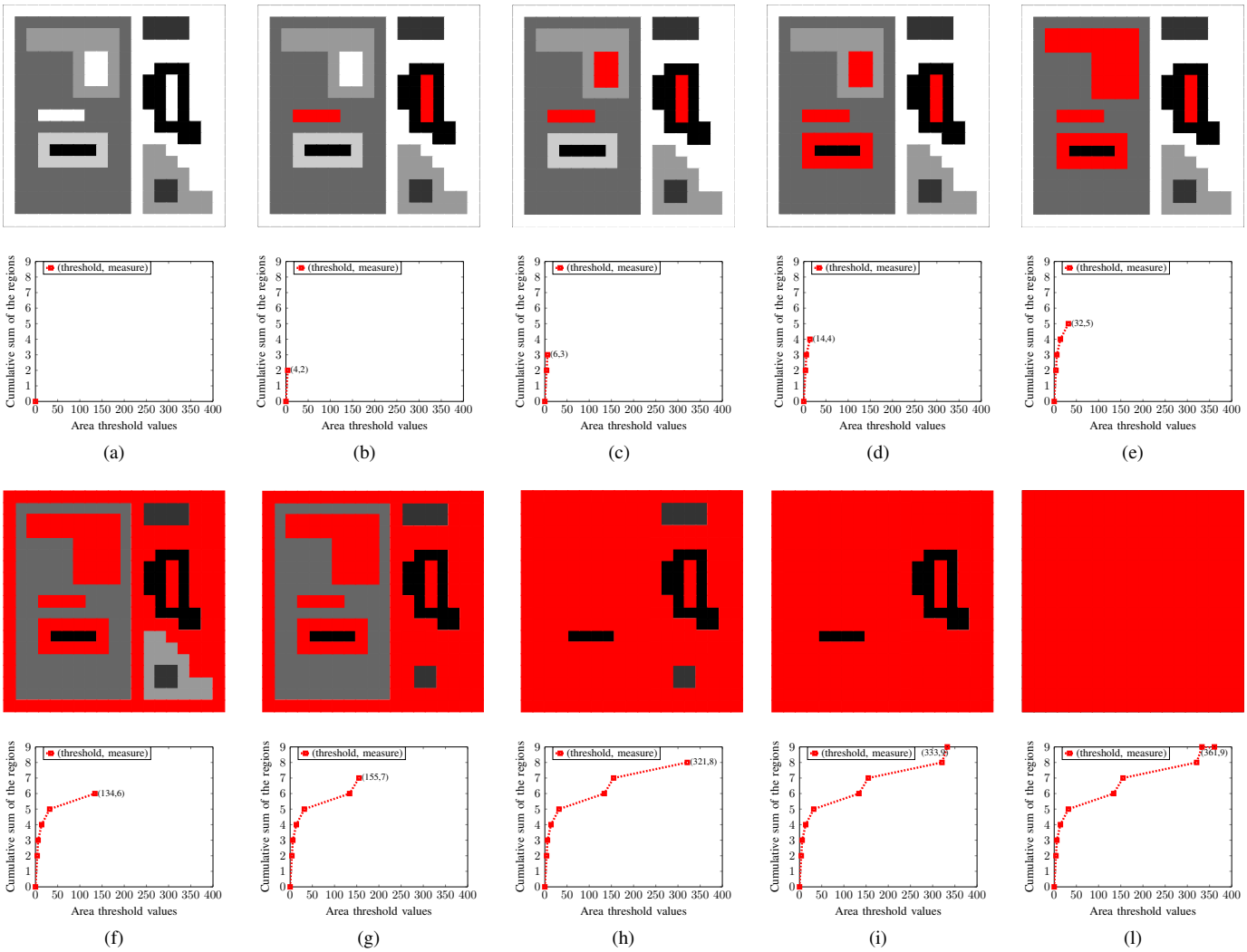

(a) (b) (c) (d) (e)

(f) (g) (h) (i) (l)

Fig. 3. Example of a GCF computed on a toy image by considering the number of changed regions as measure. The figure shows the effect of the filtering on the toy image and the evolution of the GCF for each possible threshold.

trend appears, i.e., where the curvature is changing. The segmentation points are then exploited to derive the candidate thresholds by projecting the breakpoints over the x-axis (see Fig. 9). For more details on the piecewise linear regression approach, the Authors encourage the Reader to consult the work in [43].

The proposed method implements two possible strategies for the selection of the final subset: a) the size, $\hat{L}$, of the subset, $\hat{\Lambda}$, is provided by the user as input threshold for the regression model; b) the final number of thresholds is automatically identified according to the estimation error. Focusing on the second strategy, the automatic thresholds identification is based on an iterative analysis of the estimation error computed in terms of the normalized root mean squared error (NRMSE) between the original GCF, which is obtained by considering the full set $\bar{\Lambda}$, and the G$\hat{\text{C}}$F computed for an increasing number of thresholds, nth, starting from $nth = 1$. As shown in Fig. 9, the estimation error curve decreases when more thresholds are considered, showing a L-shape distribution, i.e., a monotone decreasing curve that becomes stable after a certain point located in the elbow region of the curve. The aim of the iterative procedure is to identify such point, which corresponds to the one of maximum curvature. A simple pseudo-code that shows the entire procedure for the automatic strategy is described in Algorithm 1. The algorithm takes as input the 2D gray-scale image f, the tree $\mathcal{T}$, the attribute $\mathcal{A}$ and the measure $\mathcal{M}$. For each input, various options are given in brackets. Due to the nature of the employed regression model, the first and the last breakpoints correspond to the first threshold (i.e., equal to 0, resulting in the original input image) and to the last threshold (resulting in all pixels having the same gray-scale value), respectively, which do not provide useful information (see Fig. 3) and thus discarded.

Algorithm 1: Thresholds selection

input : 2D grayscale image f,
Tree $\mathcal{T}$ ('min-tree','max-tree','ToS'),
Attribute $\mathcal{A}$ ('area','standard deviation',etc.),
Measure $\mathcal{M}$ ('val','pix','reg')
output: A set of thresholds $\hat{\Lambda}$

Computation of tree representation $\mathcal{T}(f)$;
Computation of attribute $\mathcal{A}(\mathcal{T})$ on nodes;
$\{\lambda_i\}_{i=1}^{L} \longleftarrow$ sort($\mathcal{A}(\mathcal{T})$);
for $i = 1$ *to* L **do**
  G$\hat{\text{C}}$F($\mathcal{P}_{\psi_{\lambda_i}}(f)$) $\longleftarrow \mathcal{M}(\psi_{\lambda_i}(\mathcal{T}))$
end
Initialization: $nth \longleftarrow 1$;
while *elbow position is not stable* **do**
  Estimation of G$\hat{\text{C}}$F($\mathcal{P}_{\psi}(f), nth$);
  G$\hat{\text{C}}$F$_{interp}$ $\longleftarrow$ Interpolation of G$\hat{\text{C}}$F over $\bar{\Lambda}$;
  $err_{nth} \longleftarrow 1-$NRMSE(GCF, G$\hat{\text{C}}F_{interp}$);
  if $nth > 1$ **then**
    compute the elbow position of **err**;
  end
  $nth \longleftarrow nth + 1$;
end
$\hat{L} \longleftarrow nth$;
$\hat{\Lambda} \longleftarrow \{\hat{\lambda}_i\}_{z=1}^{\hat{L}}$;

V. Experimental Analysis

Aiming at comparing the proposed approach with other existing strategies, the experimental analysis is carried out on two real remote sensing data sets and the performance is evaluated in terms of classification accuracies. It worths to note that the proposed selection method is unsupervised, which means that no class information is used in the selection procedure. For instance, the set of the selected thresholds and its associated features might not be discriminative of objects belonging to different classes. Therefore, the comparison with [38] is partly unfair since it make use of information of the labeled samples (i.e., training set). Anyway the experimental results show the flexibility of the proposed approach in providing complementary contextual information as a support for a classification problem.

A. Data set description

1) Rome: The data set is composed by panchromatic and multispectral (blue, green, red and near IR) channels acquired by QuickBird satellite sensor over the city of Rome, Italy. The data size is 1188 $\times$ 972 pixels with a geometrical resolution of $0.65\,\mathrm{m}$ in panchromatic and of $2.62\,\mathrm{m}$ in multispectral. The acquired scene is a dense heterogeneous urban area, which includes 9 ground reference classes, namely: buildings, blocks, roads, light train, vegetation, trees, bare soil, soil, towers. The data set and the related reference map are shown in Figs. 4a and 4b, respectively, while the class information is reported in Table I. This data set is considered challenging due to the oblique acquisition angle and the presence of long shadows. Pansharpening was applied to the panchromatic and multispectral channels using the Undecimated Discrete Wavelet Transform method [52].

2) Pavia: The data set is a hyperspectral image acquired by ROSIS-03 (Reflective Optics Imaging Spectrometer) airborne sensor over the university area of the city of Pavia, Italy. The sensor has 115 data channels with a spectral coverage ranging from 0.43 to $0.86\,\mu\mathrm{m}$. After removing 12 noisy data channels, the final data set counts 103 spectral bands, showing an area of 610 $\times$ 340 pixels with a geometrical resolution of $1.3\,\mathrm{m}$. The ground-truth includes nine classes of interest, namely: asphalt, meadow, gravel, trees, metal sheets,bare soil, bitumen, self-blocking bricks and shadows. The data set and the related reference map are shown in Figs. 4c - 4e, while the class information is reported in Table I.

B. Experimental setup

For each data set, the profiles derived from the different tree structures (min-tree, max tree and ToS) are computed as described in Section III-C for both the attributes of *area* and *standard deviation*.

In the case of Pavia data set and, more in general, when hyperspectral images are analysed, performing the morphological decomposition considering the full spectral dimension

(a) (b) (c) (d) (e)

Fig. 4. Rome data set: (a) true colour image and (b) reference data. Pavia University data set: (c) true colour image; (d) test set and (e) training set.

TABLE I
CLASSES AND NUMBERS OF TRAINING AND TEST SAMPLES FOR ROME AND PAVIA DATA SETS.

Rome				Pavia			
No.	Class	Training	Test	No.	Class	Training	Test
1	Buildings	18126	163129	1	Asphalt	548	6304
2	Blocks	10982	98834	2	Meadow	540	18146
3	Roads	16353	147176	3	Gravel	392	1815
4	Light train	1606	14454	4	Trees	524	2912
5	Vegetation	6962	62655	5	Metal sheets	265	1113
6	Trees	9088	81792	6	Bare soil	532	4572
7	Bare soil	8127	73144	7	Bitumen	375	981
8	Soil	1506	13551	8	Self-blocking bricks	514	3364
9	Towers	4792	43124	9	Shadows	231	795

TABLE II
THE SIZE L OF THE FULL SETS OF VALUES $\bar{\Lambda} = \{\lambda_i\}_{i=1}^{L}$ FOR EACH DATA SET, DIFFERENT TREE REPRESENTATIONS AND ATTRIBUTES.

f	$\mathcal{A}$	min-tree	max-tree	ToS
Panch.	area	3206	5337	5910
	standard deviation	109	212	210
1st pc	area	1907	1823	2302
	standard deviation	90	212	208
2nd pc	area	1191	1972	2181
	standard deviation	67	111	108
3rd pc	area	970	944	1124
	standard deviation	87	74	89
4th pc	area	365	398	431
	standard deviation	32	62	73

is not feasible. In such case, dimensionality reduction is commonly applied in order to derive a sub-set of few feature on which perform the multi-scale morphological feature extraction. In our experiment analysis, dimensionality reduction is performed via principal component analysis retaining the first four principal components (pc) corresponding to the highest eigenvalues.

Table II reports the size L of the full sets of possible thresholds $\bar{\Lambda} = \{\lambda_i\}_{i=1}^{L}$ (i.e., the full set of attribute values) that characterize each data set. The thresholds used to extract the final profile are automatically selected by employing the automatic strategy described in Section IV-B, which is based on the estimation error analysis, and using the measures detailed in Section IV-A.

For the classification task, a random forest algorithm is employed as supervised learning algorithm with the number of trees set at 200. In the case of Roma data set, the classification results are obtained by performing a 10-fold cross-validation with random selection of the training set to be the 10 % of the reference samples, while the remaining samples are used as test set. For such data set, mean values and standard deviations of the classification results are computed and reported in the final analysis. In the case of Pavia data set, both the training and testing sets are available in the literature and considered fixed.

Furthermore, the classification results obtained by exploiting the proposed approach are compared against those obtained from tree strategies available in the literature and presented in [39] (hereafter Gha13), [38] (hereafter Mar13) and [37] (hereafter Mah12), taking into account their context of application (e.g., Mar13 is an approach developed to work with the *standard deviation* attribute, therefore is not included in the analysis when the *area* attribute is used). The methods are briefly described in Sec. II.

C. Results and discussion

In this section, the experimental results are presented and discussed for each data set. For Rome data set, we report in Fig. 9 the estimated $\hat{\text{GCF}}$s for the ToS and each measure,

TABLE III
CLASSIFICATION RESULTS OBTAINED FOR ROME DATA SET. EACH PROFILE IS BUILT ON THE PANCHROMATIC IMAGE CONSIDERING THE ATTRIBUTE *area*. FOR EACH METHOD AND PROFILE, THE TABLE REPORTS THE AVERAGE OF 10-FOLD CROSS-VALIDATION PROCEDURE OF THE PERCENTAGE OVERALL ACCURACIES OA(%), THE PERCENTAGE AVERAGE ACCURACIES AA(%) AND THE KAPPA COEFFICIENTS *K*, WITH RELATIVE STANDARD DEVIATIONS SHOWN IN BRACKETS.

	GCF_{val}	GCF_{pix}	GCF_{reg}	Gha13	
No. features	5	5	4	15	
$\mathcal{P}_\phi$	26.81 (0.22)	34.34 (0.13)	**40.66 (0.14)**	37.28 (0.16)	AA
	42.46 (0.16)	49.58 (0.11)	**54.16 (0.05)**	52.33 (0.11)	OA
	28.73 (0.27)	37.78 (0.11)	**44.30 (0.11)**	41.76 (0.15)	K
No. features	5	5	4	15	
$\mathcal{P}_\gamma$	57.33 (0.69)	**67.31 (0.18)**	59.43 (0.16)	68.88 (0.19)	AA
	62.56 (0.35)	**71.68 (0.08)**	63.57 (0.05)	70.62 (0.09)	OA
	54.42 (0.48)	**65.91 (0.11)**	56.01 (0.07)	64.58 (0.11)	K
No. features	9	9	7	29	
$\mathcal{AP}$	55.34 (0.49)	75.96 (0.17)	65.86 (0.14)	**77.94 (0.13)**	AA
	61.90 (0.32)	78.21 (0.06)	69.95 (0.07)	**78.25 (0.09)**	OA
	53.55 (0.41)	73.96 (0.08)	64.03 (0.08)	**74.12 (0.11)**	K
No. features	6	**3**	4	15	
$\mathcal{P}_\rho$	**82.57 (0.14)**	67.36 (0.32)	72.26 (0.12)	77.91 (0.18)	AA
	84.27 (0.06)	76.59 (0.15)	75.41 (0.04)	79.76 (0.08)	OA
	81.25 (0.07)	71.90 (0.19)	70.63 (0.05)	75.77 (0.11)	K
No. features	5 + 4	5 + 4	4 + 4	15 + 4	
$\mathcal{P}_\phi$ + MS	69.24 (0.13)	73.60 (0.09)	**73.78 (0.09)**	73.25 (0.11)	AA
	74.93 (0.06)	78.84 (0.06)	79.12 (0.04)	**79.14 (0.04)**	OA
	69.89 (0.07)	74.67 (0.07)	75.01 (0.05)	**75.03 (0.05)**	K
No. features	5 + 4	5 + 4	4 + 4	15 + 4	
$\mathcal{P}_\gamma$ + MS	85.75 (0.11)	**89.45 (0.09)**	81.14 (0.11)	87.62 (0.06)	AA
	86.08 (0.04)	**89.75 (0.04)**	82.87 (0.05)	87.67 (0.03)	OA
	83.43 (0.06)	**87.81 (0.05)**	79.56 (0.07)	85.33 (0.04)	K
No. features	9 + 4	9 + 4	7 + 4	29 + 4	
$\mathcal{AP}$ + MS	82.21 (0.18)	91.15 (0.11)	84.78 (0.11)	**91.39 (0.11)**	AA
	83.84 (0.11)	**91.99 (0.06)**	86.75 (0.04)	91.80 (0.05)	OA
	80.70 (0.14)	**90.48 (0.07)**	84.22 (0.04)	90.27 (0.06)	K
No. features	6 + 4	**3 + 4**	4 + 4	15 + 4	
$\mathcal{P}_\rho$ + MS	**94.18 (0.07)**	90.87 (0.12)	85.42 (0.12)	92.74 (0.09)	AA
	94.72 (0.04)	92.41 (0.05)	87.36 (0.07)	92.93 (0.03)	OA
	93.73 (0.05)	90.98 (0.06)	84.95 (0.09)	91.61 (0.04)	K

TABLE IV
CLASSIFICATION RESULTS OBTAINED FOR ROME DATA SET. EACH PROFILE IS BUILT ON THE PANCHROMATIC IMAGE CONSIDERING THE ATTRIBUTE *standard deviation*. FOR EACH METHOD AND PROFILE, THE TABLE REPORTS THE AVERAGE OF 10-FOLD CROSS-VALIDATION PROCEDURE OF THE PERCENTAGE OVERALL ACCURACIES OA(%), THE PERCENTAGE AVERAGE ACCURACIES AA(%) AND THE KAPPA COEFFICIENTS *K*, WITH RELATIVE STANDARD DEVIATIONS SHOWN IN BRACKETS.

	GCF_{val}	GCF_{pix}	GCF_{reg}	Gha13	Mar13	
No. features	3	2	6	12	5	
$\mathcal{P}_\phi$	20.25 (2.64)	32.78 (0.12)	39.62 (0.09)	**42.89 (0.16)**	28.91 (0.21)	AA
	38.23 (1.81)	46.63 (0.09)	53.25 (0.05)	**56.68 (0.07)**	44.76 (0.18)	OA
	20.92 (3.28)	34.51 (0.11)	43.03 (0.09)	**47.25 (0.08)**	31.49 (0.24)	K
No. features	6	4	8	12	5	
$\mathcal{P}_\gamma$	63.55 (0.44)	63.20 (0.11)	70.17 (0.21)	**70.48 (0.13)**	68.43 (0.15)	AA
	68.00 (0.21)	66.40 (0.06)	**70.92 (0.05)**	70.51 (0.04)	70.66 (0.11)	OA
	61.39 (0.25)	59.55 (0.08)	**64.99 (0.08)**	64.55 (0.07)	64.71 (0.14)	K
No. features	8	5	13	23	9	
$\mathcal{AP}$	55.32 (1.77)	66.09 (0.11)	75.95 (0.08)	**78.19 (0.12)**	69.55 (0.25)	AA
	64.42 (0.51)	68.75 (0.06)	76.55 (0.04)	**79.07 (0.09)**	72.07 (0.11)	OA
	56.74 (0.66)	62.58 (0.08)	71.98 (0.05)	**74.96 (0.11)**	66.34 (0.14)	K
No. features	4	**5**	7	12	5	
$\mathcal{P}_\rho$	73.53 (0.29)	78.05 (0.12)	**80.13 (0.14)**	80.26 (0.13)	74.05 (0.28)	AA
	76.23 (0.17)	80.23 (0.06)	**81.01 (0.08)**	80.98 (0.07)	76.54 (0.16)	OA
	71.60 (0.21)	76.45 (0.07)	**77.39 (0.11)**	77.26 (0.08)	71.86 (0.19)	K
No. features	3 + 4	2 + 4	6 + 4	12 + 4	5 + 4	
$\mathcal{P}_\phi$ + MS	67.60 (0.12)	71.80 (0.12)	73.40 (0.12)	**74.41 (0.09)**	70.83 (0.08)	AA
	73.85 (0.08)	76.79 (0.03)	78.61 (0.05)	**79.80 (0.04)**	76.21 (0.03)	OA
	68.59 (0.11)	72.20 (0.04)	74.40 (0.06)	**75.83 (0.05)**	71.50 (0.04)	K
No. features	6 + 4	4 + 4	8 + 4	12 + 4	5 + 4	
$\mathcal{P}_\gamma$ + MS	87.70 (0.08)	83.29 (0.08)	86.28 (0.09)	86.43 (0.07)	**87.74 (0.05)**	AA
	88.56 (0.03)	84.73 (0.06)	86.60 (0.05)	87.31 (0.05)	88.50 (0.04)	OA
	86.39 (0.04)	81.81 (0.07)	84.04 (0.06)	84.89 (0.06)	86.32 (0.05)	K
No. features	8 + 4	5 + 4	13 + 4	23 + 4	9 + 4	
$\mathcal{AP}$ + MS	86.33 (0.07)	85.51 (0.13)	88.51 (0.07)	**89.46 (0.07)**	86.18 (0.11)	AA
	87.79 (0.05)	86.63 (0.08)	89.22 (0.04)	**90.76 (0.04)**	87.87 (0.05)	OA
	85.47 (0.07)	84.09 (0.11)	87.17 (0.05)	**89.00 (0.05)**	85.55 (0.06)	K
No. features	4 + 4	**5 + 4**	7 + 4	12 + 4	5 + 4	
$\mathcal{P}_\rho$ + MS	88.74 (0.06)	**91.14 (0.09)**	90.36 (0.11)	90.06 (0.06)	89.60 (0.08)	AA
	90.06 (0.07)	**92.22 (0.05)**	91.26 (0.08)	91.06 (0.02)	90.64 (0.06)	OA
	88.18 (0.08)	**90.76 (0.06)**	89.61 (0.11)	89.36 (0.03)	88.87 (0.08)	K

showing the selected thresholds used for building the relative profile considering the attribute *area*. Moreover, for each estimated $\hat{\text{GCF}}$, the relative estimation error, which provides the size of the final threshold set, is also provided. It is worth noting that by employing the Algorithm 1, the point selected on the curve represents a trade-off between the size of the threshold set and the minimum estimation error. In each $\hat{\text{GCF}}$'s graph, the line composed by blue dots represents the real GCF (computed with the full set of thresholds), the red line denotes the estimated $\hat{\text{GCF}}$ and yellow circles identifies the breakpoints, which are used to derive the thresholds for building the profile. It can be seen that each GCF, computed by considering a different measure, describes a certain behaviour of the morphological decomposition, and thus, provides a different set of thresholds.

Considering the Rome data set, the classification results of the experiments in which the attribute *area* is employed are shown in Table III. The table shows the results obtained by the proposed approach for the three GCFs (i.e., GCF_{val}, GCF_{pix}, GCF_{reg}), and those obtained by Gha13 method. First, the experimental analysis is conducted by considering the only panchromatic channel, and later, the analysis is extended to include the spectral channels in the feature space. In both scenarios, it can be seen that by employing the $\mathcal{P}_\phi$ or $\mathcal{P}_\gamma$ profiles alone leads to poor classification accuracies. This is due to the fact that both the attribute opening and attribute closing profiles extract partial information of the scene, related to dark and bright regions, respectively. Such behaviour is also explained by the high complexity and heterogeneity of the scene, in particular for the class *building*, which is characterized by an high spectral variability (gray-level range of values). The classification results are improved when the attribute opening and closing are considered as part of the same structure, as it is in the case of $\mathcal{AP}$. By using such operator, the opening and closing profiles derived by the min-tree and max-tree representations are concatenated, providing complementary information, but requiring a higher number of thresholds for the estimation of $\hat{\text{GCF}}$s. A further improvement is achieved by employing the ToS representation to obtain the $\mathcal{P}_\rho$ profiles, which obtains the highest classification accuracy. The $\mathcal{P}_\rho$ performs the morphological decomposition considering dark and bright regions at the same time, making this operator more adaptable to different gray-levels conditions. By comparing the different methods, it is important to notice that the proposed method creates, in general, profiles characterized by a very small number of features, while obtaining classifica-

TABLE V
CLASSIFICATION RESULTS OBTAINED FOR PAVIA DATA SET. EACH PROFILE IS BUILT ON THE FIRST FOUR PRINCIPAL COMPONENTS CONSIDERING THE ATTRIBUTE *area*. FOR EACH METHOD AND PROFILE, THE TABLE REPORTS THE PERCENTAGE OVERALL ACCURACIES OA(%), THE PERCENTAGE AVERAGE ACCURACIES AA(%) AND THE KAPPA COEFFICIENTS *K*.

	GCF_{val}	GCF_{pix}	GCF_{reg}	Gha13	Mah12	
No. features	16	21	18	60	36	
$E\mathcal{P}_\phi$	76.67	83.57	83.45	84.16	**85.77**	AA
	77.72	79.70	**81.82**	79.79	80.84	OA
	70.85	73.27	**75.70**	73.55	74.80	K
No. features	17	13	16	60	36	
$E\mathcal{P}_\gamma$	85.96	86.65	84.90	**88.59**	87.57	AA
	75.08	**86.48**	75.87	85.50	82.25	OA
	68.86	**82.41**	69.84	81.25	77.35	K
No. features	29	30	30	116	68	
$E\mathcal{AP}$	85.63	89.79	85.50	**93.07**	91.15	AA
	76.54	88.04	80.91	**91.25**	88.08	OA
	70.49	84.01	74.88	**88.46**	84.27	K
No. features	19	16	14	60	36	
$E\mathcal{P}_\rho$	93.73	**94.22**	85.75	91.88	88.39	AA
	94.01	**94.34**	83.58	91.06	85.08	OA
	91.82	**92.33**	78.12	88.12	80.33	K

TABLE VI
CLASSIFICATION RESULTS OBTAINED FOR PAVIA DATA SET. EACH PROFILE IS BUILT ON THE FIRST FOUR PRINCIPAL COMPONENTS CONSIDERING THE ATTRIBUTE *standard deviation*. FOR EACH METHOD AND PROFILE, THE TABLE REPORTS THE PERCENTAGE OVERALL ACCURACIES OA(%), THE PERCENTAGE AVERAGE ACCURACIES AA(%) AND THE KAPPA COEFFICIENTS *K*.

	GCF_{val}	GCF_{pix}	GCF_{reg}	Gha13	Mah12	Mar13	
No. features	13	14	16	48	36	19	
$E\mathcal{P}_\phi$	79.54	83.16	83.42	**84.79**	82.87	76.42	AA
	74.55	78.90	**78.94**	78.22	73.40	75.29	OA
	67.10	**72.28**	72.17	71.57	66.09	67.36	K
No. features	21	18	15	48	36	19	
$E\mathcal{P}_\gamma$	**93.84**	90.26	85.59	89.35	84.91	89.97	AA
	90.89	89.07	85.99	88.46	84.09	**91.41**	OA
	88.05	85.68	81.76	84.88	79.46	**88.60**	K
No. features	30	28	27	92	68	34	
$E\mathcal{AP}$	**93.83**	90.34	88.11	91.27	87.98	88.83	AA
	92.01	88.62	86.18	89.43	85.04	88.92	OA
	89.48	84.87	81.62	85.98	80.14	85.44	K
No. features	13	16	18	48	36	19	
$E\mathcal{P}_\rho$	**95.18**	92.40	89.29	91.64	87.83	89.15	AA
	90.94	**91.35**	90.00	87.79	86.07	89.57	OA
	88.15	**88.25**	86.37	83.65	81.38	85.78	K

tion accuracies that are better or similar to those obtained by Gha13 method. The classification maps corresponding to the best results achieved by each technique are shown in Fig. 5.

The classification results obtained by considering the *standard deviation* attribute are shown in Table IV. The obtained results have a similar trend to those obtained with the attribute *area*. As in the previous case, when the $\mathcal{P}_\phi$ or $\mathcal{P}_\gamma$ are used alone, they achieve the lowest classification accuracies, while by employing the $\mathcal{AP}$ and $\mathcal{P}_\rho$, the results are improved. For this case, we report the accuracies achieved by the Gha13 and Mar13 methods. From the comparison it can be observed that all the methods achieved very similar classification results. However, the proposed approach requires less features compared to the Gha13, while Mar13 provides profiles of similar size. Fig. 6 shows the classification maps corresponding to the best results achieved by each technique considered in the comparison.

For the Pavia data set, the results of the attribute *area* are reported in Table V. Unlike the Rome data set, the use of $\mathcal{P}_\phi$ or $\mathcal{P}_\gamma$ profiles provide already good classification results. Such accuracies are slightly improved by exploiting the $\mathcal{AP}$ and in particular the $\mathcal{P}_\rho$, which provided the best classification accuracies. For comparison, the Gha13 and Mah12 methods are considered. From the table, it can be seen that our approach is able to achieve better or similar results than those obtained by the Gha13 and Mah13 by creating low dimensional profiles. The classification maps corresponding to the best results achieved by each technique are shown in Fig. 7.

The classification results obtained for the same data set using the *standard deviation* attribute are listened in Table VI. Also in this case, it can be seen the effectiveness of the proposed approach in providing the highest classification accuracies (except when the $\mathcal{P}_\gamma$ is used) while providing profiles charactered by a low number of features. In contrast, Gha13, Mah12 and Mar13 identify profiles characterized by a high number of features without improving the final classification results. Fig. 8 shows the classification maps corresponding to the best results achieved by each technique.

VI. CONCLUSIONS

This paper presented an approach for the computation of morphological attribute profiles, which relies on a novel framework for the automatic selection the filters' thresholds[3]. The automatic selection procedure is based on Granulometric Characteristic Functions, a generalization of the conventional granulometric curve. Three GCFs have been defined based on different measures, such as the sum of the gray-level values, the number of pixels and the number of regions affected by the filtering. The motivation for using different GCFs relies on the fact that the filtering effects in the image decomposition are represented according to different characteristics (e.g., in terms of variations of contrast, scale of the areas affected by filtering, etc). GCFs have been then considered in the threshold selection strategy. Specifically, the proposed selection algorithm allows to retrieve the set of thresholds whose associated GCF better approximates the GCF computed with all possible thresholds. It worths noting that the exploitation of tree representations (i.e., component trees or ToS) allows us to compute the GCFs directly from the tree representation. This is a great advantage since manual (i.e., trial & error) and existing automatic strategies need to actually filter an image for carrying out the threshold selection. This is unpractical for real applications due to the potentially high cardinality of the set of all possible filter thresholds, resulting in a suboptimal exploration of the domain of the filter parameters.

Experiments were conducted addressing a scene classification problem in order to make a comparison with other

[3]The Matlab executable files of the proposed method are provided at http://www.openremotesensing.net

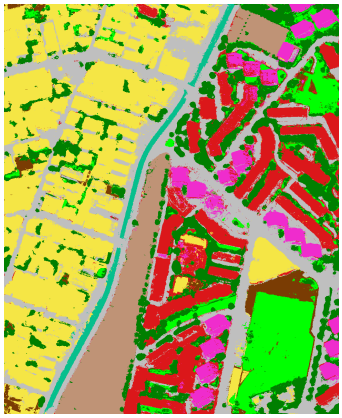

(a) GCF$_{val}$ (OA 94.72)

(b) Gha13 (OA 92.93)

Fig. 5. Classification maps of Roma data set for the experiments reported in Table III (area attribute): (a-b) $\mathcal{P}_\rho$ + MS.

(a) GCF$_{pix}$ (OA 92.22)

(b) Gha13 (OA 91.06)

(c) Mar13 (OA 90.64)

Fig. 6. Classification maps of Rome data set for the experiments reported in Table IV (standard deviation attribute): (a-b-c) $\mathcal{P}_\rho$ + MS.

threshold selection methods available in the literature. The comparison showed the effectiveness of the proposed approach in achieving overall higher classification accuracies and, at the same time, in providing more representative profiles composed of a lower number of filtered images. This fact is particularly advantageous because leads to a further reduction of the computational cost since the image analysis is performed in a feature space of lower dimensionality. The experimental results showed also that, considering the proposed automatic strategy, overall the attribute profiles computed on the three of shapes lead to a better representation (in terms of classification accuracy) of the image content with respect to those based on component trees.

Several aspects would deserve a more in depth analysis starting from this work. For example, the choice of the GCF used for the selection seems to be dependent on the scene and on the filter used for computing the profiles. In this regard, we plan a deeper investigation on the effects of different GCFs in the representation of the image content. Decision fusion strategies could be employed if one wants to consider multiple GCFs in the analysis. Another interesting future developments is the investigation of threshold selection when considering jointly different attributes. Furthermore, despite the suitability of the proposed selection technique for computing an attribute profile used in a supervised analysis of an image, the selection procedure is fully unsupervised. We plan to better address the supervised classification scenario by designing a selection technique that integrates the a priori information available in the scene.

REFERENCES

[1] P. Teeninga, U. Moschini, S. C. Trager, and M. H. F. Wilkinson, "Statistical Attribute Filtering to Detect Faint Extended Astronomical Sources," *Mathematical Morphology - Theory and Applications*, vol. 1, no. 1, pp. 100–115, 1 2016.

[2] D. L. Pham, C. Xu, and J. L. Prince, "Current Methods in Medical Image Segmentation," *Annual Review of Biomedical Engineering*, vol. 2, no. 1, pp. 315–337, 2000.

[3] M. Li, S. Zang, B. Zhang, S. Li, and C. Wu, "A Review of Remote Sensing Image Classification Techniques: The Role of Spatio-Contextual Information," *European Journal of Remote Sensing*, vol. 47, no. 1, pp. 389–411, 2014.

[4] X. Kang, S. Li, L. Fang, and J. A. Benediktsson, "Intrinsic image decomposition for feature extraction of hyperspectral images," *IEEE Transactions on Geoscience and Remote Sensing*, vol. 53, no. 4, pp. 2241–2253, April 2015.

[5] J. P. Serra, *Image Analysis and Mathematical Morphology*, 1982, vol. 1. [Online]. Available: http://books.google.ch/books?id=6pZTAAAAYAA

(a) GCF$_{pix}$ (OA 94.34) (b) Gha13 (OA 91.25) (c) Mah12 (OA 88.08)

Fig. 7. Classification maps of Pavia data set for the experiments reported in Table V (area attribute): (a) E$\mathcal{P}_\rho$ and (b-c) E$\mathcal{AP}$.

(a) GCF$_{val}$ (OA 92.01) (b) Gha13 (OA 89.43) (c) Mah12 (OA 86.07) (d) Mar13 (OA 89.57)

Fig. 8. Classification maps of Pavia data set for the experiments reported in Table VI (standard deviation attribute): (a-b) E$\mathcal{AP}$, (c) E$\mathcal{P}_\rho$ and (d) E$\mathcal{P}_\gamma$.

[6] P. Soille and M. Pesaresi, "Advances in Mathematical Morphology Applied to Geoscience and Remote Sensing," *IEEE Transactions on Geoscience and Remote Sensing*, vol. 40, no. 9, pp. 2042–2055, 2002.

[7] C. Berger, T. Geraud, R. Levillain, N. Widynski, A. Baillard, and E. Bertin, "Effective Component Tree Computation with Application to Pattern Recognition in Astronomical Imaging," in *Proceedings of the IEEE International Conference on Image Processing*, vol. 4, 2007, pp. IV – 41–IV – 44.

[8] E. Carlinet and T. Géraud, "MToS: A Tree of Shapes for Multivariate Images," *IEEE Transactions on Image Processing*, vol. 24, no. 12, pp. 5330–5342, 2015.

[9] E. R. Urbach, "Intelligent Object Detection Using Trees," in *Mathematical Morphology and Its Application to Signal and Image Processing - Proc. of the 12h Intl. Symp. on Mathematical Morphology (ISMM)*, J. A. Benediktsson, J. Chanussot, L. Najman, and H. Talbot, Eds. Springer International Publishing, 2015, pp. 289–300.

[10] L. Najman and J. Cousty, "A Graph-based Mathematical Morphology Reader," *Pattern Recogn. Lett.*, vol. 47, pp. 3–17, Oct. 2014.

[11] J. B. Kruskal, "On the Shortest Spanning Subtree of a Graph and the Traveling Salesman Problem," *Proceedings of the American Mathematical Society*, vol. 7, pp. 48–50, 1956.

[12] G. K. Ouzounis and P. Soille, "The Alpha-Tree Algorithm," 2012.

[13] P. Salembier and L. Garrido, "Binary Partition Tree as an Efficient Representation for Image Processing, Segmentation, and Information Retrieval," *IEEE Transactions on Image Processing*, vol. 9, no. 4, pp. 561–576, 2000.

[14] R. Jones, "Component Trees for Image Filtering and Segmentation," in *Procedings of IEEE Workshop on Nonlinear Signal and Image Processing (NISP)*, E. Coyle, Ed., Mackinac Island, sep 1997.

[15] P. Salembier, A. Oliveras, and L. Garrido, "Antiextensive Connected Operators for Image and Sequence Processing," *IEEE Transactions on Image Processing*, vol. 7, no. 4, pp. 555–570, 1998.

[16] V. Caselles, B. Coll, and J. M. Morel, "Topographic Maps and Local Contrast Changes in Natural Images," *International Journal of Computer Vision*, vol. 33, no. 1, pp. 5–27, 1999.

[17] J. A. Benediktsson, L. Bruzzone, J. Chanussot, M. Dalla Mura, P. Salembier, and S. Valero, "Hierarchical Analysis of Remote Sensing Data: Morphological Attribute Profiles and Binary Partition Trees," in *Lecture Notes in Computer Science (including subseries Lecture Notes in Artificial Intelligence and Lecture Notes in Bioinformatics)*, vol. 6671 LNCS,

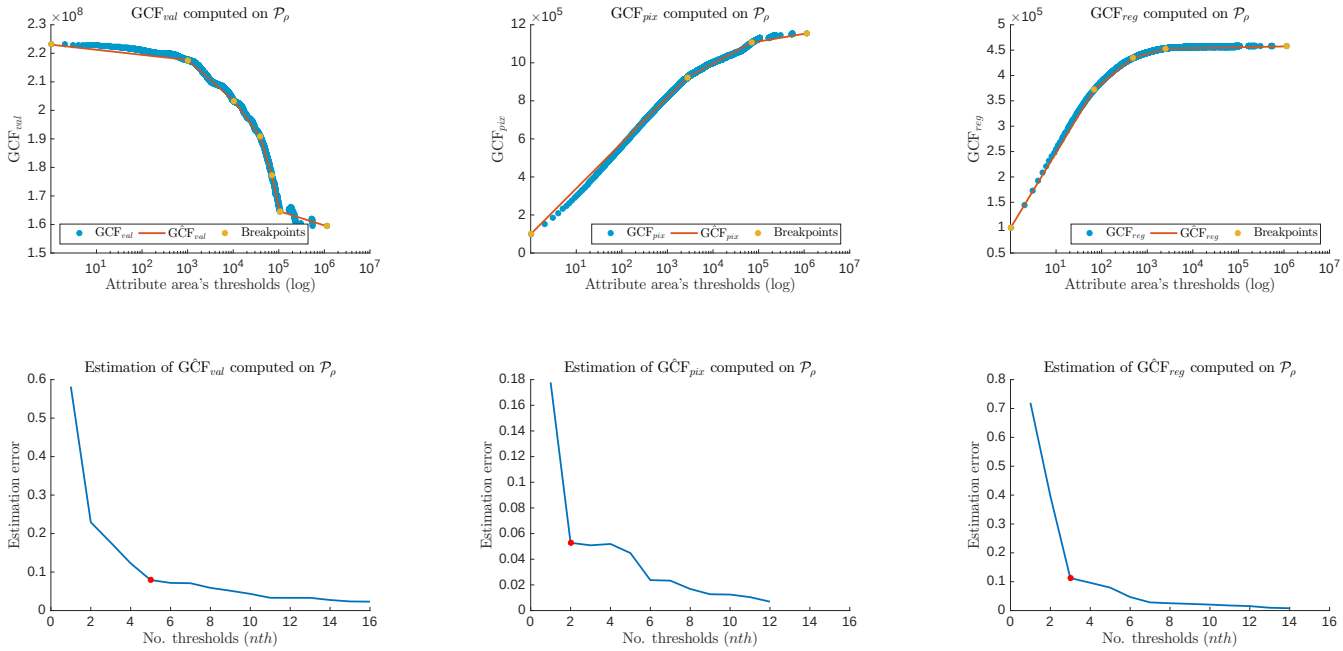

Fig. 9. GCFs derived for Rome data set considering the following measures: (from left to right) number of gray-values, number of changed pixels and number of changed region. The GCFs are computed for the ToS (top row). For each GCF the estimation error (bottom row) is also depicted, showing the number of threshold chosen for the GCF estimation. For each GCF the red line denotes the estimated GĈF and yellow circles identifies the breakpoints, which are used to derive the final set of thresholds.

2011, pp. 306–319.

[18] E. J. Breen and R. Jones, "Attribute Openings, Thinnings, and Granulometries," *Computer Vision and Image Understanding*, vol. 64, no. 3, pp. 377–389, nov 1996.

[19] M. Dalla Mura, J. A. Benediktsson, B. Waske, and L. Bruzzone, "Morphological Attribute Filters for the Analysis of Very High Resolution Remote Sensing Images," in *IEEE International Geoscience and Remote Sensing Symposium (IGARSS '09)*, vol. 3, 2009, pp. 2–3.

[20] P. Teeninga, U. Moschini, S. C. Trager, and M. H. F. Wilkinson, "Improved Detection of Faint Extended Astronomical Objects Through Statistical Attribute Filtering," in *Mathematical Morphology and Its Applications to Signal and Image Processing (ISMM): 12th International Symposium*, J. A. Benediktsson, J. Chanussot, L. Najman, and H. Talbot, Eds. Springer International Publishing, 2015, pp. 157–168.

[21] I. K. E. Purnama, K. Y. E. Aryanto, and M. H. F. Wilkinson, "Non-Compactness Attribute Filtering to Extract Retinal Blood Vessels in Fundus Images," *International Journal of E-Health and Medical Communications (IJEHMC)*, vol. 1, no. 3, pp. 16–27, Jul. 2010.

[22] F. N. Kiwanuka and M. H. F. Wilkinson, "Automatic Attribute Threshold Selection for Morphological Connected Attribute Filters," *Pattern Recognition*, vol. 53, no. C, pp. 59–72, May 2016.

[23] P. Salembier and J. Serra, "Flat Zones Filtering, Connected Operators, and Filters by Reconstruction," *IEEE Transactions on Image Processing*, vol. 4, no. 8, pp. 1153–1160, 1995.

[24] M. Dalla Mura, J. A. Benediktsson, B. Waske, and L. Bruzzone, "Morphological Attribute Profiles for the Analysis of Very High Resolution Images," *IEEE Transactions on Geoscience and Remote Sensing*, vol. 48, no. 10, pp. 3747–3762, 2010.

[25] M. Dalla Mura, J. A. Benediktsson, and L. Bruzzone, "Self-dual Attribute Profiles for the Analysis of Remote Sensing Images," in *Mathematical Morphology and Its Application to Signal and Image Processing - Proc. of the 10h Intl. Symp. on Mathematical Morphology (ISMM)*, P. Soille, M. Pesaresi, and G. Ouzounis, Eds. Springer Berlin Heidelberg, 2011, pp. 320–330.

[26] G. Cavallaro, M. Dalla Mura, J. A. Benediktsson, and A. Plaza, "Remote Sensing Image Classification Using Attribute Filters Defined over the Tree of Shapes," *IEEE Transactions on Geoscience and Remote Sensing*, 2016.

[27] M. Dalla Mura, J. Atli Benediktsson, B. Waske, and L. Bruzzone, "Extended Profiles with Morphological Attribute Filters for the Analysis of Hyperspectral Data," pp. 5975–5991, 2010.

[28] G. Cavallaro, M. Dalla Mura, J. A. Benediktsson, and L. Bruzzone, "Extended Self-Dual Attribute Profiles for the Classification of Hyperspectral Images," *IEEE Geoscience and Remote Sensing Letters*, vol. 99, pp. 1–5, 2015.

[29] B. Song, M. Dalla Mura, P. Li, A. J. Plaza, J. M. Bioucas-Dias, J. A. Benediktsson, and J. Chanussot, "Remotely Sensed Image Classification Using Sparse Representations of Morphological Attribute Profiles," *IEEE Transactions on Geoscience and Remote Sensing*, vol. 52, no. 8, pp. 5122–5136, aug 2014.

[30] P. Quesada-Barriuso, F. Arguello, and D. B. Heras, "Spectral-Spatial Classification of Hyperspectral Images Using Wavelets and Extended Morphological Profiles," *IEEE Journal of Selected Topics in Applied Earth Observations and Remote Sensing*, vol. 7, no. 4, pp. 1177–1185, 2014.

[31] Z. Zhong, B. Fan, J. Duan, L. Wang, K. Ding, S. Xiang, and C. Pan, "Discriminant Tensor Spectral-Spatial Feature Extraction for Hyperspectral Image Classification," *IEEE Geoscience and Remote Sensing Letters*, vol. 12, no. 5, pp. 1028–1032, may 2015.

[32] N. Falco, J. A. Benediktsson, and L. Bruzzone, "Spectral and Spatial Classification of Hyperspectral Images Based on ICA and Reduced Morphological Attribute Profiles," *IEEE Transactions on Geoscience and Remote Sensing*, vol. 53, no. 11, pp. 6223–6240, nov 2015.

[33] M. Pedergnana, P. R. Marpu, M. Dalla Mura, J. A. Benediktsson, and L. Bruzzone, "Classification of Remote Sensing Optical and LiDAR Data Using Extended Attribute Profiles," *IEEE Journal of Selected Topics in Signal Processing*, vol. 6, no. 7, pp. 856–865, nov 2012.

[34] N. Falco, M. Dalla Mura, F. Bovolo, J. A. Benediktsson, and L. Bruzzone, "Study on the Capabilities of Morphological Attribute Profiles in Change Detection on VHR Images," in *Proc. SPIE 7830, Image and Signal Processing for Remote Sensing XVI*, L. Bruzzone, Ed., vol. 7830. Toulouse: International Society for Optics and Photonics, sep 2010, pp. 783 010–783 016.

[35] N. Falco, M. D. Mura, F. Bovolo, J. A. Benediktsson, and L. Bruzzone, "Change Detection in VHR Images Based on Morphological Attribute Profiles," *IEEE Geoscience and Remote Sensing Letters*, vol. 10, no. 3, pp. 636–640, 2013.

[36] G. K. Ouzounis, M. Pesaresi, and P. Soille, "Differential Area Profiles:

Decomposition Properties and Efficient Computation," *IEEE Transactions on Pattern Analysis and Machine Intelligence*, vol. 34, no. 8, pp. 1533–1548, 2012.
[37] Z. Mahmood, G. Thoonen, and P. Scheunders, "Automatic Threshold Selection for Morphological Attribute Profiles," in *Proceedings of the IEEE International Geoscience and Remote Sensing Symposium (IGARSS)*, 2012, pp. 4946–4949.
[38] P. R. Marpu, M. Pedergnana, M. Dalla Mura, J. A. Benediktsson, and L. Bruzzone, "Automatic Generation of Standard Deviation Attribute Profiles for Spectral-Spatial Classification of Remote Sensing Data," *IEEE Geoscience and Remote Sensing Letters*, vol. 10, no. 2, pp. 293–297, 2013.
[39] P. Ghamisi, J. A. Benediktsson, and J. R. Sveinsson, "Automatic SpectralSpatial Classification Framework Based on Attribute Profiles and Supervised Feature Extraction," *IEEE Transactions on Geoscience and Remote Sensing*, pp. 1–12, 2013.
[40] G. Franchi and J. Angulo, "Morphological Principal Component Analysis for Hyperspectral Image Analysis," Tech. Rep., 2016.
[41] P. Soille, *Morphological Image Analysis*, 2nd ed. Berlin, Heidelberg: Springer Berlin Heidelberg, 2004.
[42] L. Najman and H. Talbot, *Mathematical Morphology: From Theory to Applications*. ISTE-Wiley, jun 2010.
[43] D. Lemire, "A Better Alternative to Piecewise Linear Time Series Segmentation," *Arxiv preprint cs0605103*, vol. 2007, pp. 545–550, 2006. [Online]. Available: http://arxiv.org/abs/cs/0605103
[44] P. Maragos, "Pattern Spectrum and Multiscale Shape Representation," *IEEE Transactions on Pattern Analysis and Machine Intelligence*, vol. 11, no. 7, pp. 701–716, 1989.
[45] E. R. Urbach, J. B. T. M. Roerdink, and M. H. F. Wilkinson, "Connected Shape-Size Pattern Spectra for Rotation and Scale-Invariant Classification of Gray-Scale Images," *IEEE Transactions on Pattern Analysis and Machine Intelligence*, vol. 29, no. 2, pp. 272–285, 2007.
[46] R. Jones, "Connected Filtering and Segmentation Using Component Trees," *Computer Vision and Image Understanding*, vol. 75, no. 3, pp. 215–228, sep 1999. [Online]. Available: http://www.sciencedirect.com/science/article/pii/S1077314299907774
[47] P. Monasse and F. Guichard, "Fast Computation of a Contrast-Invariant Image Representation," *IEEE Transactions on Image Processing*, vol. 9, no. 5, pp. 860–872, 2000.
[48] V. Caselles and P. Monasse, *Geometric Description of Images as Topographic Maps*, 1st ed. Springer-Verlag Berlin Heidelberg, 1984.
[49] Y. Song, "A Topdown Algorithm for Computation of Level Line Trees," *IEEE Transactions on Image Processing*, vol. 16, no. 8, pp. 2107–2116, 2007.
[50] T. Géraud, E. Carlinet, S. Crozet, and L. Najman, "A Quasi-Linear Algorithm to Compute the Tree of Shapes of nD Images," in *Lecture Notes in Computer Science (including subseries Lecture Notes in Artificial Intelligence and Lecture Notes in Bioinformatics)*, vol. 7883 LNCS, 2013, pp. 98–110.
[51] S. Crozet and T. Geraud, "A First Parallel Algorithm to Compute the Morphological Tree of Shapes of nD Images," in *Proceedings of the IEEE International Conference on Image Processing (ICIP)*, 2014, pp. 2933–2937.
[52] B. Aiazzi, L. Alparone, S. Baronti, and A. Garzelli, "Context-driven fusion of high spatial and spectral resolution images based on oversampled multiresolution analysis," *IEEE Transactions on Geoscience and Remote Sensing*, vol. 40, no. 10, pp. 2300–2312, Oct 2002.

Gabriele Cavallaro received the B.S. and M.S. degrees in telecommunications engineering from the University of Trento, Italy, in 2011 and 2013, respectively. He holds a Ph.D. degree in Electrical and Computer Engineering from the University of Iceland, obtained in 2016. At present he is a postdoctoral research assistant at the Juelich Supercomputing Centre, Juelich, Germany. At this institute, he is part of a scientific research group focused on high productivity data processing within the Federated Systems and Data Division. His research interests include remote sensing and analysis of very high geometrical and spectral resolution optical data with the current focus on mathematical morphology and high performance computing. He was the recipient of the IEEE GRSS Third Prize in the Student Paper Competition of the 2015 IEEE International Geoscience and Remote Sensing Symposium 2015 (Milan, Italy, July 2015). He serves as a reviewer for IEEE Geoscience and Remote Sensing Letters and IEEE Journal of Selected Topics in Earth Observations and Remote Sensing.

Nicola Falco (S10-M'15) received the B.Sc. and M.Sc. degrees in Telecommunication Engineering from the University of Trento, Italy, in 2008 and 2011, respectively. He holds a joint Ph.D. degree in Electrical and Computer Engineering from the University of Iceland, and in Information and Communication Technologies from the University of Trento obtained in 2015. He is currently a Postdoctoral Fellow at the Climate & Ecosystem Sciences Division (CESD), Lawrence Berkeley National Laboratory, Berkeley, California. His research interests focus on remote sensing image analysis and processing with applications in environmental monitoring and climate change. His work concentrates on the development of methodologies for data analysis and information extraction mainly in optical and hyperspectral imagery, spanning multiple disciplines, such as image and signal processing, mathematical morphology, pattern recognition and machine learning. Dr. Falco was a recipient of the Recognition of IEEE GEOSCIENCE REMOTE SENSING LETTERS BEST REVIEWERS in 2013. He was co-recipient of the IEEE GRSS third price in the Student Paper Competition of the 2015 IEEE International Geoscience and Remote Sensing Symposium.

Mauro Dalla Mura (S'08 – M'11) received the laurea (B.E.) and laurea specialistica (M.E.) degrees in Telecommunication Engineering from the University of Trento, Italy, in 2005 and 2007, respectively. He obtained in 2011 a joint Ph.D. degree in Information and Communication Technologies (Telecommunications Area) from the University of Trento, Italy and in Electrical and Computer Engineering from the University of Iceland, Iceland. In 2011 he was a Research fellow at Fondazione Bruno Kessler, Trento, Italy, conducting research on computer vision. He is currently an Assistant Professor at Grenoble Institute of Technology (Grenoble INP), France. He is conducting his research at the Grenoble Images Speech Signals and Automatics Laboratory (GIPSA-Lab). His main research activities are in the fields of remote sensing, image processing and pattern recognition. In particular, his interests include mathematical morphology, classification and multivariate data analysis. Dr. Dalla Mura was the recipient of the IEEE GRSS Second Prize in the Student Paper Competition of the 2011 IEEE IGARSS 2011 and co-recipient of the Best Paper Award of the International Journal of Image and Data Fusion for the year 2012-2013 and the Symposium Paper Award for IEEE IGARSS 2014. Dr. Dalla Mura is the President of the IEEE GRSS French Chapter since 2016 (he previously served as Secretary 2013-2016). He is on the Editorial Board of IEEE Journal of Selected Topics in Applied Earth Observations and Remote Sensing (J-STARS) since 2016.

Jón Atli Benediktsson (S'84-M'90-SM'99-F'04) received the Cand.Sci. degree in electrical engineering from the University of Iceland, Reykjavik, in 1984, and the M.S.E.E. and Ph.D. degrees in electrical engineering from Purdue University, West Lafayette, IN, in 1987 and 1990, respectively. On July 1, 2015 he became the Rector of the University of Iceland. From 2009 to 2015 he was the Pro Rector of Science and Academic Affairs and Professor of Electrical and Computer Engineering at the University of Iceland. His research interests are in remote sensing, biomedical analysis of signals, pattern recognition, image processing, and signal processing, and he has published extensively in those fields. Prof. Benediktsson was the 2011-2012 President of the IEEE Geoscience and Remote Sensing Society (GRSS) and has been on the GRSS AdCom since 2000. He was Editor in Chief of the IEEE Transactions on Geoscience and Remote Sensing (TGRS) from 2003 to 2008 and has served as Associate Editor of TGRS since 1999, the IEEE Geoscience and Remote Sensing Letters since 2003 and IEEE Access since 2013. He is on the Editorial Board of the Proceedings of the IEEE, the International Editorial Board of the International Journal of Image and Data Fusion and was the Chairman of the Steering Committee of IEEE Journal of Selected Topics in Applied Earth Observations and Remote Sensing (J-STARS) 2007-2010. Prof. Benediktsson is a co-founder of the biomedical start up company Oxymap (www.oxymap.com). He is a Fellow of the IEEE and a Fellow of SPIE. Prof. Benediktsson is a member of the 2014 IEEE Fellow Committee. He received the Stevan J. Kristof Award from Purdue University in 1991 as outstanding graduate student in remote sensing. In 1997, Dr. Benediktsson was the recipient of the Icelandic Research Council's Outstanding Young Researcher Award, in 2000, he was granted the IEEE Third Millennium Medal, in 2004, he was a co-recipient of the University of Iceland's Technology Innovation Award, in 2006 he received the yearly research award from the Engineering Research Institute of the University of Iceland, and in 2007, he received the Outstanding Service Award from the IEEE Geoscience and Remote Sensing Society. He was co-recipient of the 2012 IEEE Transactions on Geoscience and Remote Sensing Paper Award and in 2013 he was co-recipient of the IEEE GRSS Highest Impact Paper Award. In 2013 he received the IEEE/VFI Electrical Engineer of the Year Award. In 2014 he was a co-recipient of the International Journal of Image and Data Fusion Best Paper Award. He is a member of the Association of Chartered Engineers in Iceland (VFI), Societas Scinetiarum Islandica and Tau Beta Pi.